



Science Arts & Métiers (SAM)

is an open access repository that collects the work of Arts et Métiers Institute of Technology researchers and makes it freely available over the web where possible.

This is an author-deposited version published in: <https://sam.ensam.eu>
Handle ID: <http://hdl.handle.net/10985/23484>

To cite this version :

Zimo WANG, Ruiqi GUO, Qiyang MA, Faissal CHEGDANI, Bruce TAI, Satish T. S. BUKKAPATNAM, Mohamed EL MANSORI - Characterization of the physical origins of acoustic emission (AE) from natural fiber reinforced polymers (NFRPs) machining processes - The International Journal of Advanced Manufacturing Technology - Vol. 118, n°3-4, p.865-879 - 2021

Any correspondence concerning this service should be sent to the repository

Administrator : scienceouverte@ensam.eu



Characterization of the physical origins of acoustic emission (AE) from natural fiber reinforced polymers (NFRPs) machining processes

Zimo Wang¹  · Ruiqi Guo² · Qiyang Ma¹ · Faissal Chegdani^{2,3} · Bruce Tai⁴ · Mohamed El Mansori³ · Satish T. S. Bukkapatnam²

Abstract

Natural fiber reinforced polymers (NFRPs) are environmentally friendly and are receiving growing attention in the industry. However, the multi-scale structure of natural fibers and the random distribution of the fibers in the matrix material severely impede the machinability of NFRPs, and real-time monitoring is essential for quality assurance. This paper reports a synchronous in situ imaging and acoustic emission (AE) analysis of the NFRP machining process to connect the temporal features of AE to the underlying dynamics and process instability, all happen within milliseconds during the NFRP cutting. This approach allows directly observing the surface modification and chip formation from a high-speed camera (HSC) during NFRP cutting processes. The analysis of the HSC images suggests that the complex fiber structure and the random distribution introduce an unsteady, almost a freeze-and-release type motion pattern of the cutting tool with varying depths of cut at the machining interface. More pertinently, a prominent burst pattern of AE from time domain was found to emanate due to the sudden penetration of the tool into the surface of the NFRP workpiece (increasing the depth of cut), as well as a release motion of the tool from its momentary freeze position. These findings open the possibility of tracking AE signals to assess the effective specific energy and surface quality that are affected by these unsteady motion patterns.

Keywords Natural fiber reinforced polymer · Orthogonal machining · Acoustic emission characterizations

1 Introduction

Natural fiber reinforced polymers (NFRPs) have been eliciting growing interest for various industrial applications [1]. These biodegradable and recyclable materials offer tremendous economic and ecological advantages as the industry is increasingly adapting to sustainable products and manufacturing systems. However, the machining process is crucial because the

surface quality of NFRPs post-machining is a strong determinant of mechanical and acoustic properties and hence the performance and aesthetic characteristics of the NFRP products. As such materials exhibit heterogeneity in their mechanical properties on a mesoscale, their machinability is highly sensitive to the variations of the microstructure within the composites. In Fig. 1, which shows microscopy images of the surface of an NFRP sample before and after orthogonal machining, localized surface defects can be observed even under well-controlled machining conditions. These issues arise because most natural fibers are highly flexible and heterogeneous (with randomly distributed elementary fibers and/or bundled fibers) over a microscale in geometry [2]. Researchers [3] who have studied the cutting mechanism on multiple fiber material sources in reinforced plastics/samples suggest that the fiber cutting process may be highly dependent on the microstructure (how the reinforced elements/fibers are placed/ oriented within the matrix basin) and/or the mechanical properties of the matrix. Furthermore, the machining of NFRPs is complicated by the prevalence of the thermo-mechanical effect [4].

✉ Zimo Wang
zimowang@binghamton.edu

¹ Department of Systems Science and Industrial Engineering, State University of New York at Binghamton, Binghamton, NY, USA

² Department of Industrial and Systems Engineering, Texas A&M University, College Station, TX, USA

³ Arts et Métiers ParisTech, MSMP Laboratory/EA7350, Rue Saint Dominique BP508, 51006 Châlons-en-Champagne, France

⁴ Department of Mechanical Engineering, Texas A&M University, College Station, TX, USA

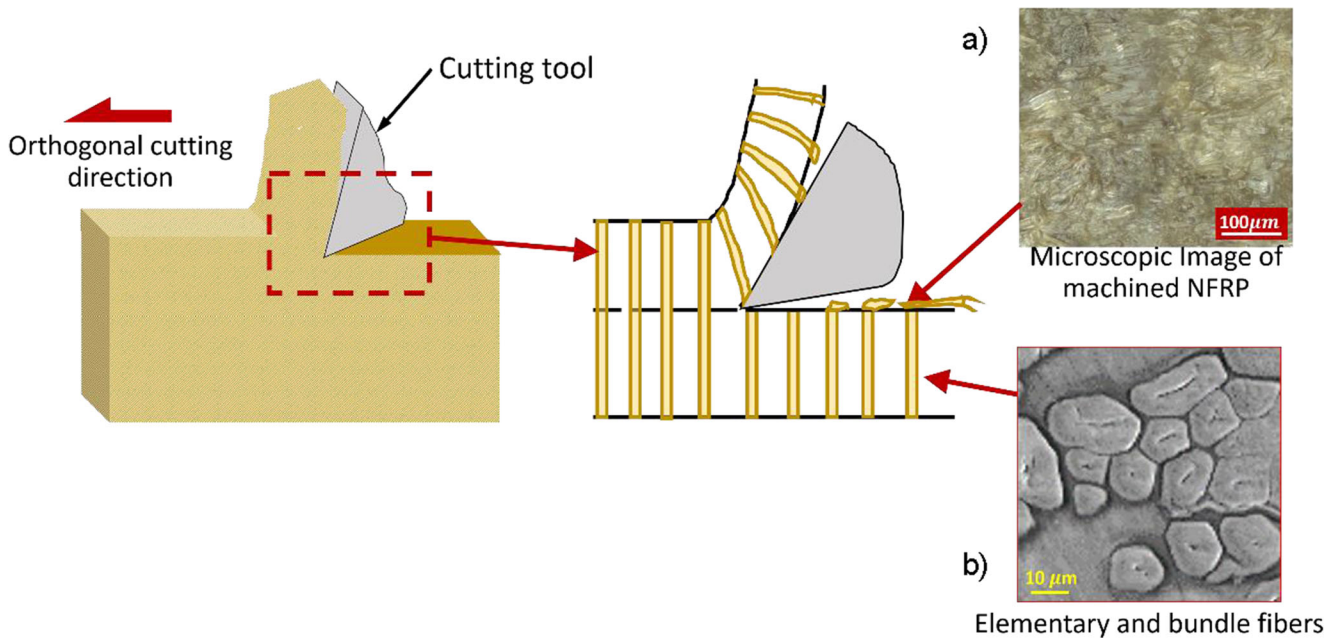


Fig. 1 A schematic diagram showing the microscopic images of NFRPs: a the machined surface with one example of an integrity issue: the prevalence of pull-out fibers; b a cross section of the NFRP showing the variations in the microstructure with elementary/bundle fiber(s)

Current investigations into characterizations of machining processes for NFRPs rely mostly on offline approaches, such as mechanical property testing and noncontact imaging/inspection, to characterize the surface integrity, multi-scale mechanical properties, chip formation, and thermo-mechanics [5–7]. However, employing these offline characterization tools is often time-consuming and hence unwieldy for real-time investigation. Therefore, a sensor-based monitoring approach is desirable to observe and characterize the diverse material removal mechanisms prevalent during NFRP cutting and to provide real-time analysis of the microdynamics as well as the surface characteristics for in-process intervention for quality control/assurance [3, 6, 8].

Acoustic emission (AE) sensors have been widely used to diagnose/test for material/structure defects. Researchers [9] have investigated the defect sizes in a rolling element bearing by analyzing the AE wavelets. Baccar and Söffke [10] also suggested that analyzing acoustic emissions is a suitable method for monitoring the health of composite structures in real time and is considered one of the most appropriate sensor-based monitoring methods, especially in dynamic systems. The acoustic emission is a transient elastic wave generated by the rapid release of energy during the plastic deformation from localized sources within and/or on the surface of a material [11]. Essentially, during the machining process, AE waveform generation is due to the phenomenon of the redistribution of the stress within the materials. Our earlier investigations [12] suggest that AE waveforms are highly associated with distinct combinations of cutting mechanism and material failure modes, such as fiber breakage and pull-outs, during the NFRP machining process. Hence, the AE sensor offers

tremendous advantages over other sensors (e.g., accelerometers and force transducers) for realizing an in-process characterization of the microdynamics (the phenomena of material failures that are peculiar to NFRP machining) and providing guidance for real-time process characterization and diagnosis, enabling timely intervention for quality assurance.

Blum and Inasaki [13] conducted experiments on machining processes to characterize the AE waveforms during materials removal. The acoustic emissions released in such a cutting zone are highly sensitive to changes in the cutting process. Rabani et al. [14] applied the AE sensor for abrasive waterjet milling processes, and the energy transfer rate of AE is used for monitoring the process. Kannatey-Asibu and Dornfeld [15] analyzed the AE signals generated during the machining process; studied the interactions between the cutting tools, the workpiece materials, and the formations; and used the AE signal analysis as a kind of online tool wear and failure detection method. Dornfeld et al. applied the AE signal in other cases, such as in the cutting test and tool wear of face milling machines [16], in the detection of the onset of motion and slip between the effector and the workpiece [17], and in tool life and surface roughness monitoring [18]. Bukkapatnam et al. [19] and Chang et al. [20] investigated the characteristics of AE waveforms sourced from the cutting zone and related them to the elastic strain rate and stress generated from/due to plastic deformation during machining. However, currently the physical sources of AE have not been fully studied for the machining of NFRP materials [12, 21]. Due to the microstructure variations of the fiber reinforced composites, failure/materials removal mechanisms are highly heterogeneous within localized regions. To connect the AE responses to the process microdynamics and/or distinct material removal

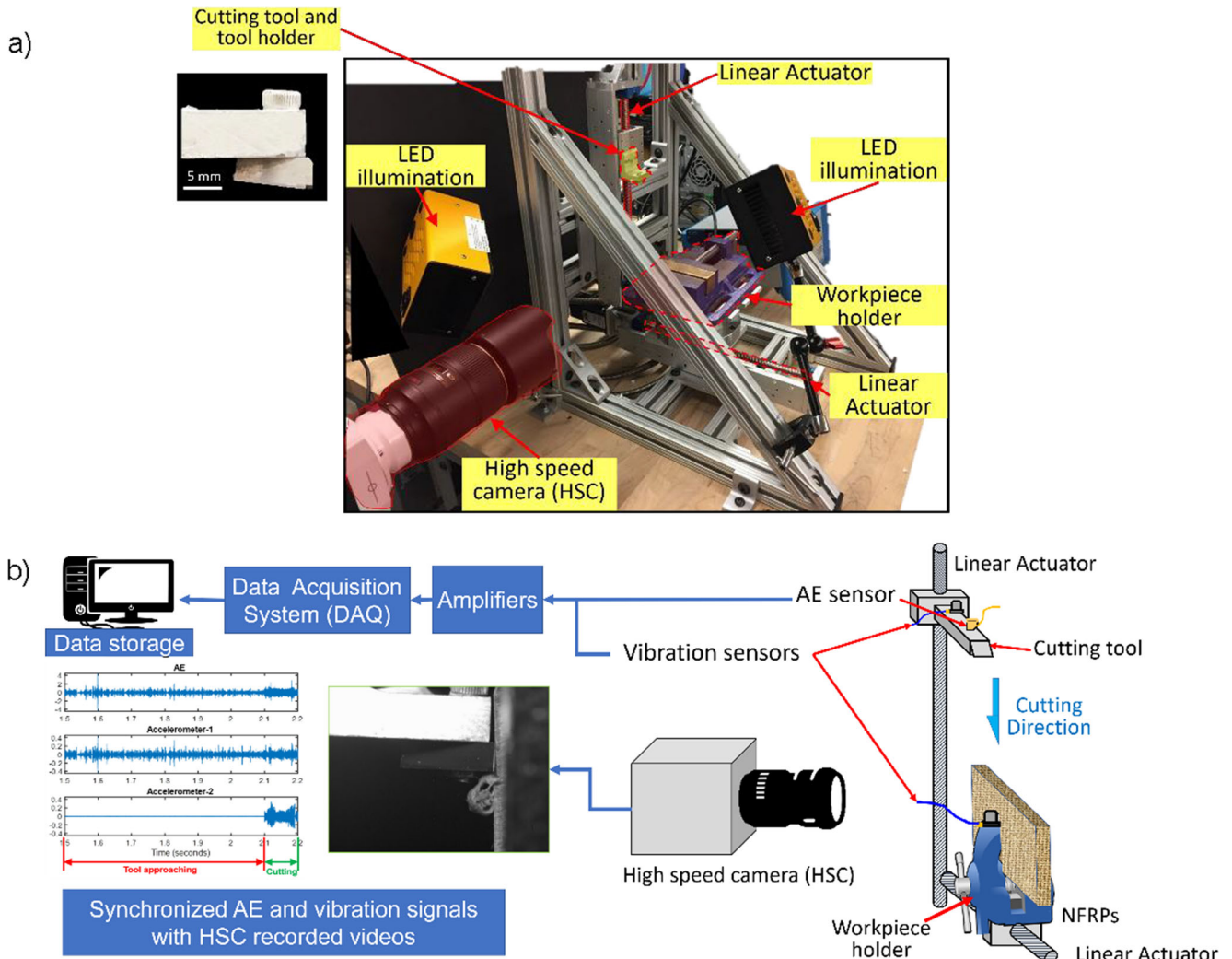


Fig. 2 The orthogonal cutting testbed for the experiment: a) the orthogonal cutting testbed with high-speed camera and the LED illumination setup; b) a schematic diagram showing the mounted sensors (two

vibration sensors and one AE sensor), the HSC, and the associated data acquisition system for gathering synchronized sensor signals and videos

mechanisms, most state-of-the-art approaches aim at unraveling the linkage between AE spectral features and different materials failure modes [22–25]. However, the time domain features of AE signals have not been fully studied for NFRP cutting—this oversight leads to the lack of instant responses of the sensor-based monitoring approach to the process microdynamics, all happened in milliseconds during the machining.

In this paper, we report an experimental study that provides direct evidence connecting the microdynamics of the machining process with the AE waveforms at a microsecond time scale. We investigate the AE signal waveforms through an orthogonal machining setup implemented with synchronous in situ imaging of the machining process and analysis of the AE signals. Our study reveals that the process microdynamics and the variations in the material’s microstructure contribute to the resultant bursty AE waveform patterns during NFRP machining. Extensive experimental case studies suggest that such phenomena have a fundamental impact on the envelope of AE waveforms. Overall, the

approach presented here allows a synchronous analysis to identify the AE waveform sources during NFRP machining.

The remainder of the paper is organized as follows: Sec. 2 details the hardware setup and experiment procedures for monitoring NFRP machining processes; Sec. 3 presents a comprehensive analytic approach for characterizing the AE waveforms with associated physical sources during the machining; the discussion and concluding remarks are in Sec. 5.

2 Experimental setup for analyzing AE characteristics via time-synchronization of sensor signals with high-speed camera video recordings

Fig. 2 shows the orthogonal testbed employed in this study [12]. This two-dimensional cutting process used a turning tool from Sandvik Coromant, with the Model TCMW16T304FLP-CD10.

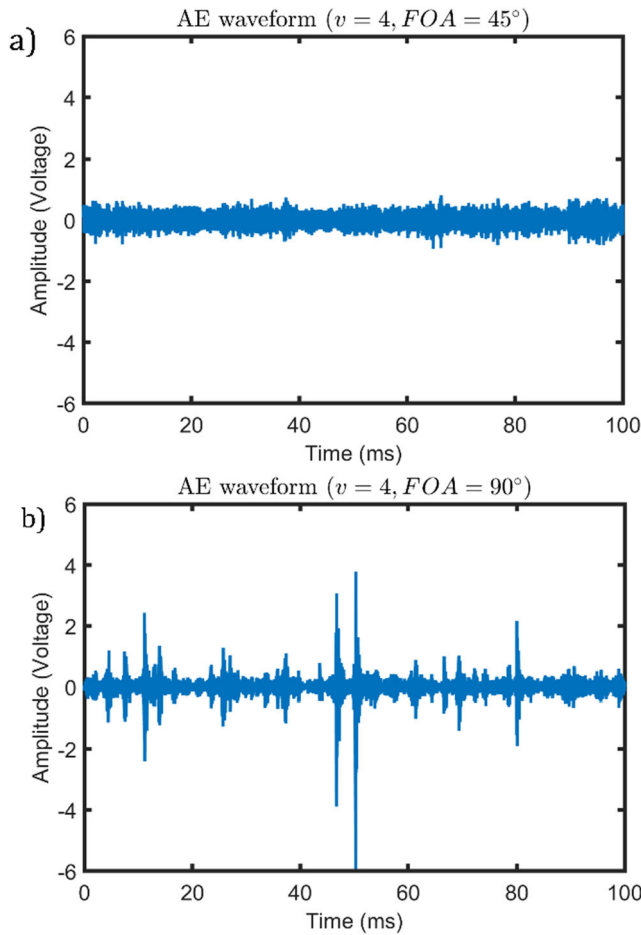


Fig. 3 The signals under the same cutting velocity ($v=4$ m/min) but with different fiber orientations: a) $FOA = 45^\circ$ and b) $FOA = 90^\circ$.

The turning tool and the associated cutting tool holder follow the standard ISO TCMW16T304FLP-CD10. The cutting tool setup was attached to a linear actuator (L70, Moog Animatics) as shown in Fig. 2. Here, an AE sensor (S9225 model from Physical Acoustics) and two accelerometers (8728A500 model from Kistler) were employed for the sensor-based in-process monitoring of the NFRP cutting. An accelerometer along with the AE sensor was placed on the cutting tool holder; the other accelerometer was placed on the workpiece holder. An NI S9223 data acquisition module was used for collecting signals with a sample rate of 1 MHz. This sampling rate allows a timely capture (at micron-second precision) of the changes via the vibration signals mounted on the workpiece holder when the cutting begins, allowing us to synchronously collect the sensor signals (AE and two vibration sensors). In total, 18 sets of experiments were conducted (with three replications for each condition except for the 90-degree angles) by choosing varying manufacturing parameters, such as cutting speed $v=2, 4, 6, 8, 10$, and 12 m/min combined with a selection of fiber orientation angles (FOA) as $FOA = 0^\circ, 45^\circ$, and 90° . Thus, 18 sets of experiments with treatment conditions of different FOA and v were conducted. All the experiments were recorded as videos using the high-

speed camera (Phantom Miro Lab310) with the resolution 640×480 pixels, a 1000 frame rate, and the exposure time of $1000 \mu s$. A macro lens (AF-S VR Micro-NIKKOR 105mm f/2.8G IF-ED Lens) was applied to zoom in on the subjects (machine tool, workpiece, and chip flow) during the experiments. Note that compared to the oblique cutting process, this two-dimensional cutting process has zero inclination angle, so the chip flows along the orthogonal plane. The high-speed camera placed normal to the orthogonal plane can capture all the phenomena (e.g., chip formation, cutting vibrations, and the process instability) during the orthogonal cutting.

From the observations of the AE signals (see Fig. 3), it may be noticed that the AE waveform envelopes exhibit distinct patterns under various machining conditions. For example, AE waveforms gathered from two different FOA s but at the same cutting speed are presented in Fig. 3: the AE waveforms under $FOA = 45^\circ$ are smoother than those at $FOA = 90^\circ$, whereas the AE envelope under $FOA = 90^\circ$ shows intermittent bursts. Our earlier investigations suggest that this phenomenon is related to the distinct combinations of cutting mechanisms under different FOA s [12]. The AE spikes (bursts) under different conditions may have the following characteristics/features: (1) the amplitudes of the AE bursts/spikes vary under different conditions (e.g., cutting speeds and/or FOA s), while the durations of different spikes are within a similar range (within milliseconds); (2) the envelopes of the spikes under the same cutting conditions have similar characteristics. The AE waveforms under $FOA = 90^\circ$ show mostly intermittent bursts, while those under other conditions, such as $FOA = 0^\circ$ or 45° at low speeds, tend to have continuous waveform patterns.

To analyze the AE signals related to the microdynamics during the cutting process, the sensor signals were synchronously coordinated one-to-one with the high-speed recordings (frame by frame). Hence, the events during the machining, such as material removal, chip formation, and interaction with the rake face of the cutting tool that all happen within millisecond(s) [3], could be synchronously connected to different waveform patterns. The following case shows the results of the HSC snapshots synchronously aligned with the AE sensor signals.

3 Observations of AE waveforms synchronized with high-speed camera video recordings from NFRP machining

Fig. 4 shows a snapshot from the high-speed camera recording along with the synchronically gathered AE signal during the NFRP machining under $v = 6$ m/min and $FOA = 90^\circ$. Here, the red arrows mark the start and the end points of the cutting process. The green lines mark the AE signal segments realized at the current cutting point. It may be noticed that the AE

Fig. 4 A snapshot via high-speed camera (HSC) aligned with synchronized AE signals—the red arrows label the start and end points of the cutting process in the video, and the parallel green lines show the start and end points of the screenshots for Spike 8

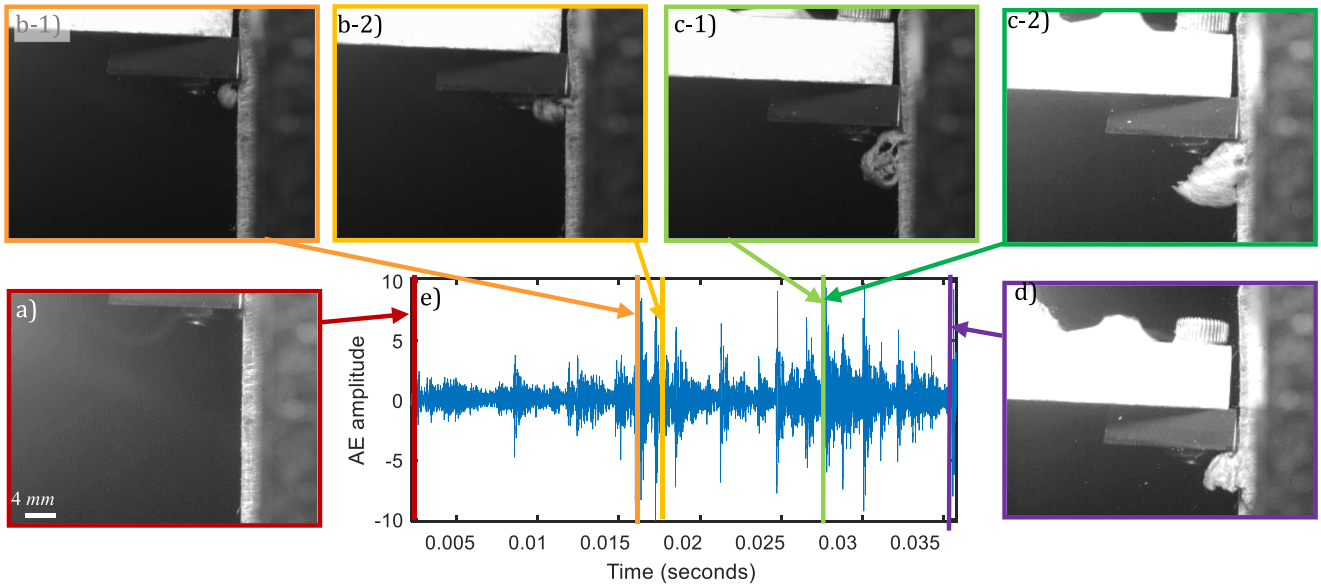
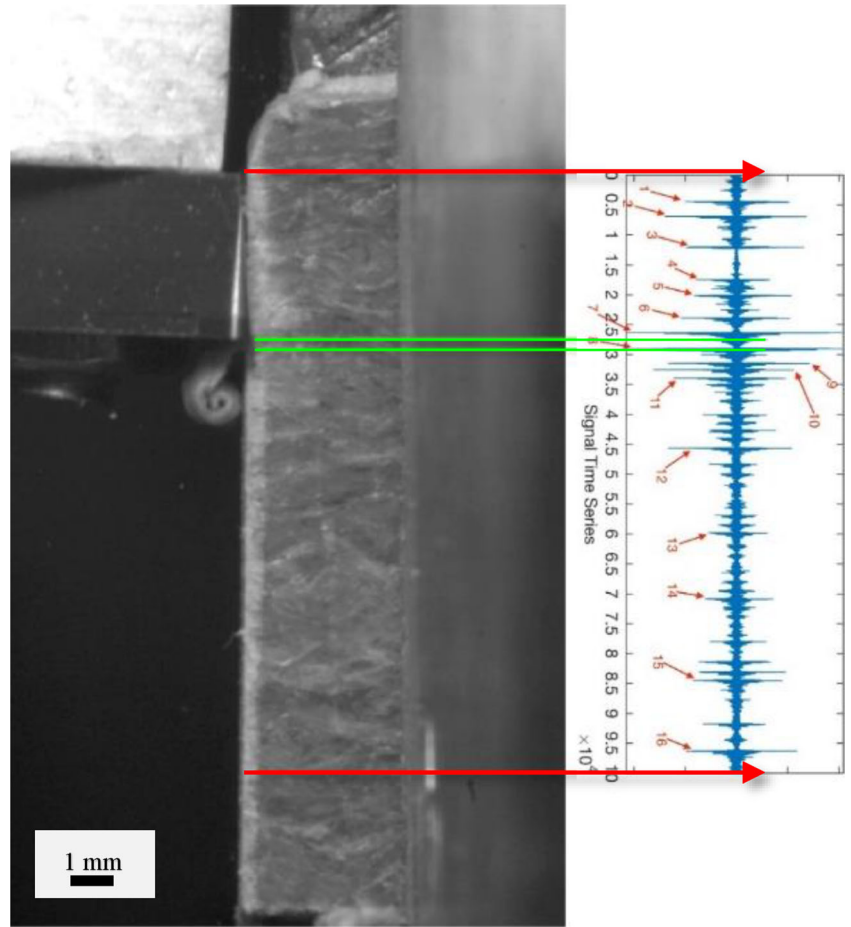


Fig. 5 The high-speed camera recording with time-synchronized AE signals during one orthogonal cutting experiment with cutting velocity $v=12$ m/min and fiber orientation of 90° : a is the initiation of the cutting; b-1 and b-2 record the emergence and propagation of a continuous chip;

snapshots (c-1 and c-2) capture the chip-tool interface during the sudden breaking away of the chip from the fiber surface; d shows the end of the cutting process, with the tool tip leaving the workpiece surface; e is the AE signal

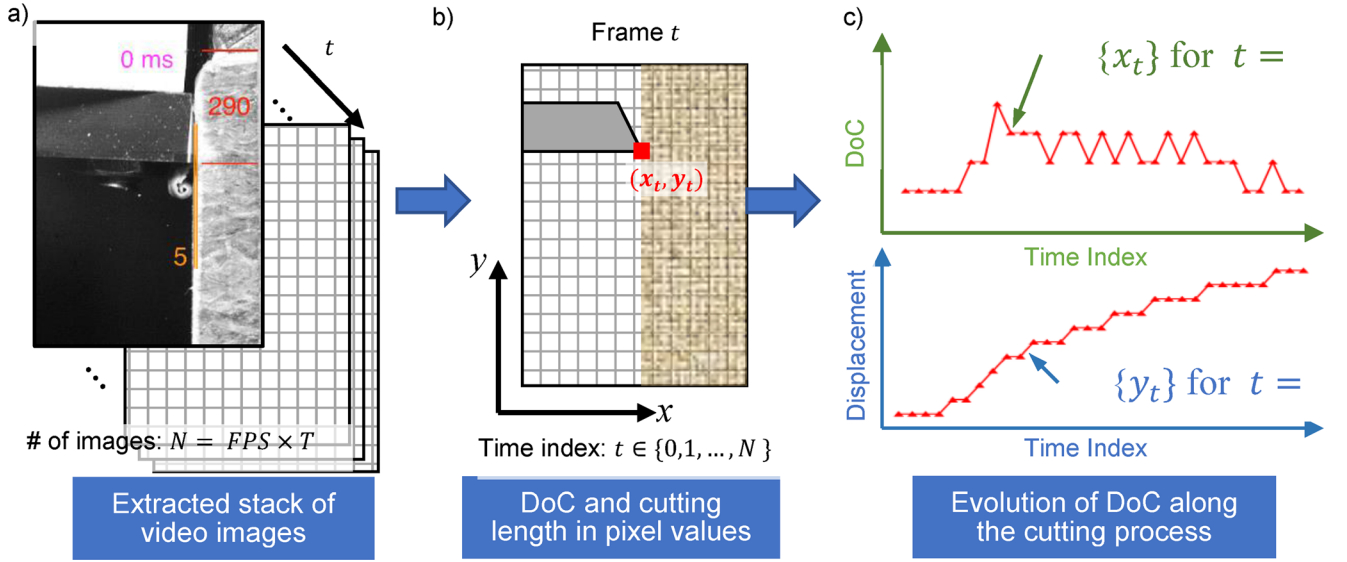


Fig. 6 A schematic diagram showing the procedure for analyzing the microdynamics of NFRP cutting via high-speed camera (HSC) recordings

waveform is marked by bursts of large spikes at the cutting point.

An illustrative example from an experiment conducted at $v = 12 \text{ m/min}$ and $FOA = 90^\circ$ is shown in Fig. 5. Sequential video snapshots (Fig. 5a to d) capture events during the chip formation and flow synchronized with the AE signals. Fig. 5a records the starting point of the cutting (cutting initiation stage) when the continuous chip emerges. As the chip emerges, it curls and starts to interact with the tool's rake surface interface. This phase is marked by irregular bursts in the AE signals (marked by orange and yellow bars in Fig. 5). Note that such AE waveform patterns may be due to the following effects: when machining is carried out at high speeds (e.g., cutting speeds of $v = 12 \text{ m/min}$), the elongation/deformation of the fibers within the basis becomes very visible (e.g., recordings with $v = 12 \text{ m/min}$) as suggested by Fig. 5 b-2. This process, in turn, creates NFRP deformation at the contact surface near the tool tip and consequently changes the geometries of the tool-workpiece interface, introducing an inconsistent depth of cut (DoC) during the process. Following chip formation and curling, the curly chip starts to break away rapidly from the fiber surface; Fig. 5 c-1 and c-2 capture two instant video frames $\sim 2 \text{ msec}$ apart of the cutting process before and after the end of a cut as the curly chip breaks. Next, the cutting tool continues to interact with the fiber surface, but no noticeable chip formation is observed till the tool tip detaches from the workpiece surface (Fig. 5d). All these sharp changes are labeled using colored bars in the time-synchronized AE signals as shown in Fig. 5e. Also, the bursts of nonstationary AE are difficult to analyze since these may be caused by multiple sources, such as the friction from the tool-chip interface and the uncertainties of the instant uncut/chip thickness. The significance of the different sources contributing to such phenomena (viz., the AE events) needs to be

further studied. The following subsections detail the procedures and the results used in investigating the connections between the nonstationary behaviors of the AE signals and the microdynamics of NFRP machining processes.

4 Analysis of experimental observations and results

Fig. 6 outlines the overall steps towards relating the AE waveform patterns to the related microdynamics of NFRP machining as gleaned from the HSC recordings. Essentially, the HSC recording is a stack of images that capture the NFRP cutting process at a millisecond time scale, and determining the coordinate values of the tool tip in consecutive frames allows a digitization to quantitatively represent the evolution of tool tip displacements as well as the DoC's. Given the time duration T (in the video recording) and the frame rate (FPS), the total number of images is expressed by $N = FPS \times T$. The pixel values, viz., the units of the digital image/ frame from the captured video, are applied as the criterion for determining the displacement and DoC during the NFRP cutting. For each image/frame at time index $t \in \{1, 2, 3, \dots, N\}$, the pixel values in both x- and y-axes allocated to the tool tip position can be extracted, where the pixel value in the x-axis (as suggested in Fig. 6b), denoted by x_t , is related to the change in DoC and the pixel value y_t in the vertical axis captures the tool tip displacement along the cutting direction. Given a sequence of the pixel values (x_t, y_t) for $t \in \{1, 2, 3, \dots, N\}$, the evolution of x_t (DoC) and y_t (tool displacement) throughout time can be represented as shown in Fig. 6c.

Based on this construct, we characterize the AE signals during the NFRP cutting process under $v = 6 \text{ m/min}$ and $FOA = 90^\circ$. In total, 16 AE waveform spikes (each is red-

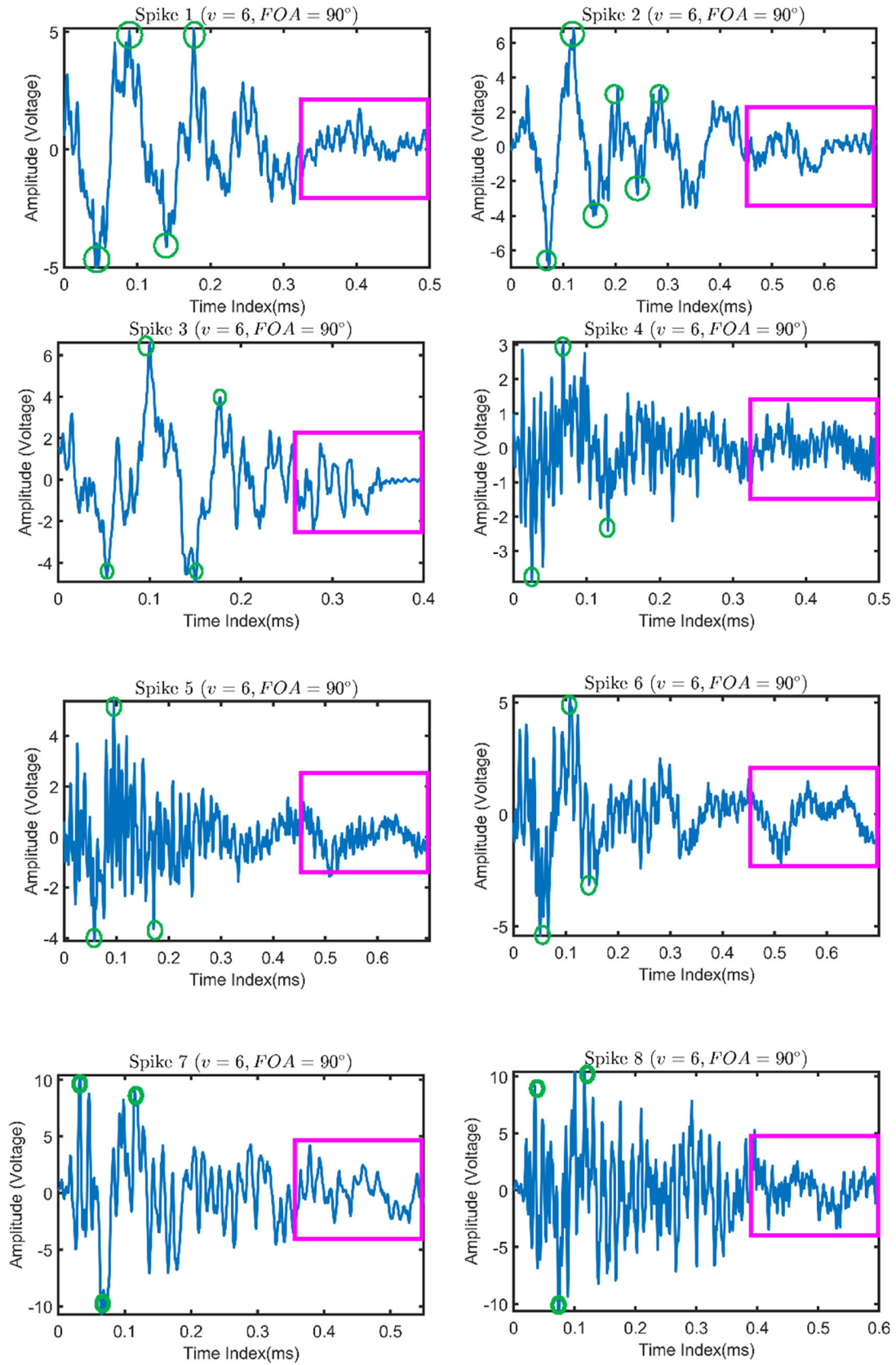


Fig. 7 A summary of 16 AE signal spikes gathered during NFRP cutting (under $v=6$ m/min and $FOA=90^\circ$)

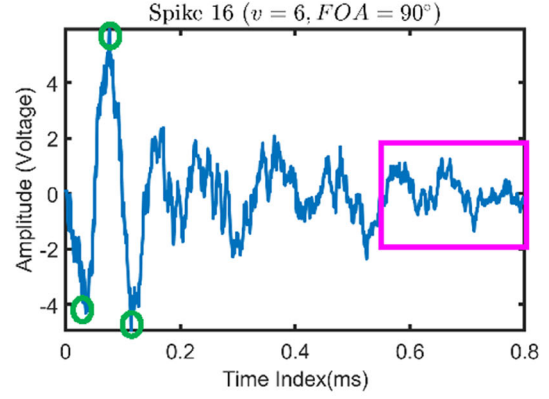
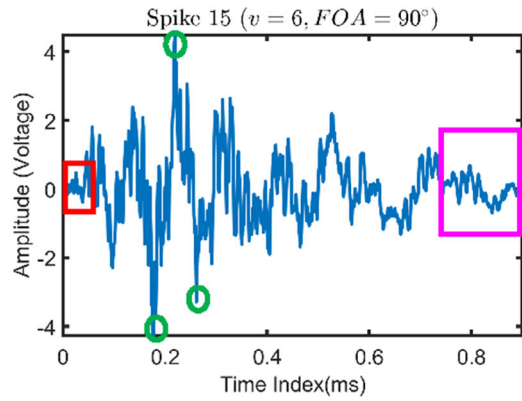
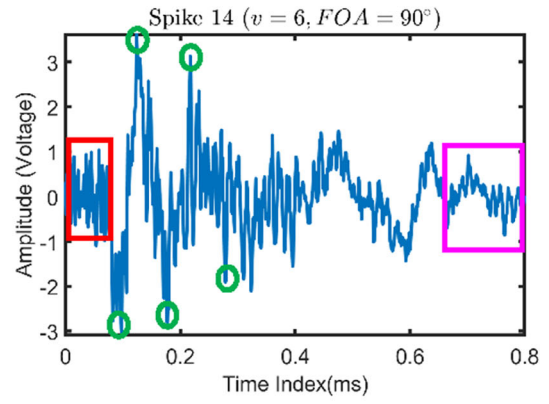
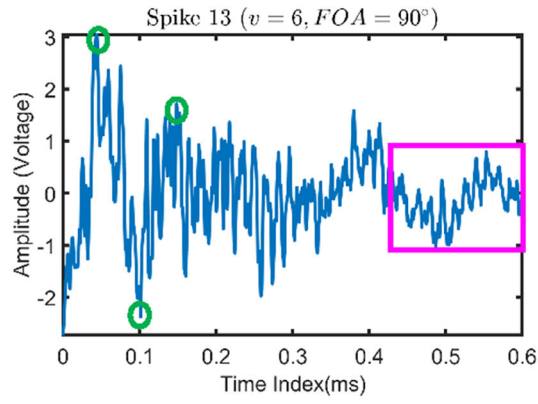
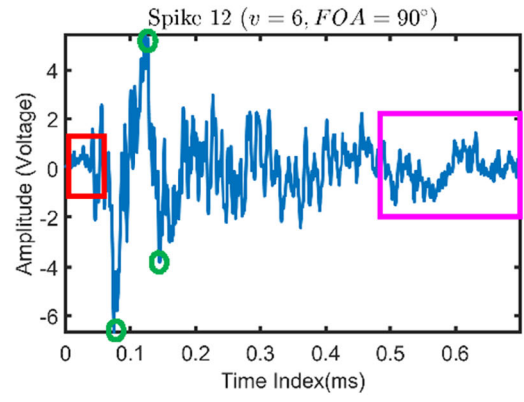
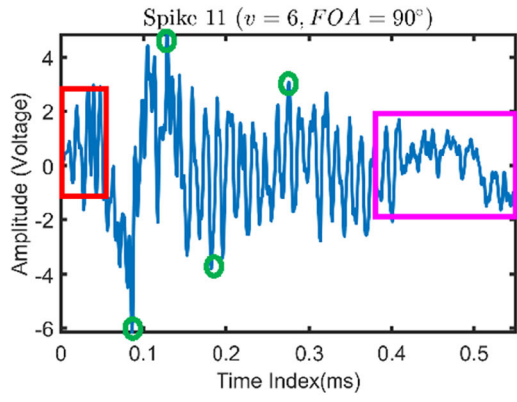
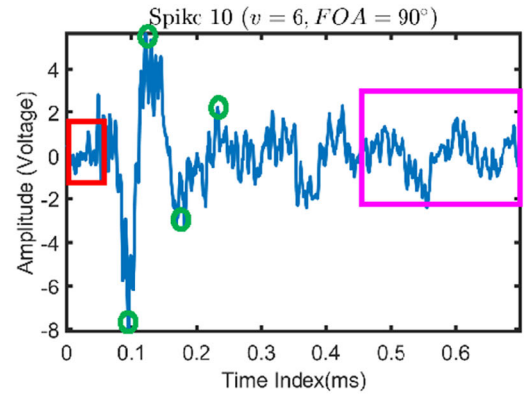
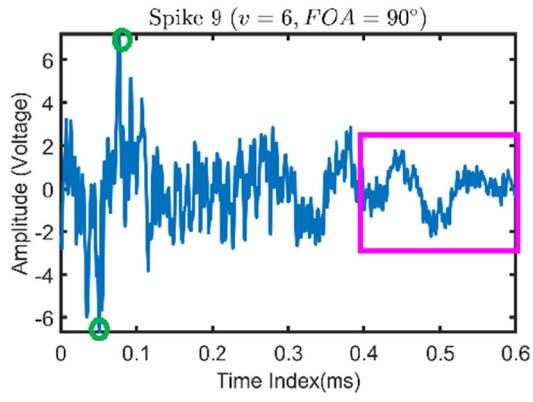


Fig. 7 (continued)

Table 1 A summary of the mathematical characteristics of 16 spikes from the cutting process with cutter velocity (v) = 6 m/min and fiber orientation (FOA) = 90°. The different colored shadings suggest two

distinct waveform patterns: the green shading indicates the Type I AE pattern, and the red color represents the Type II pattern

Spike no.	Variance	Skewness	Kurtosis	Amplitude	Range	Duration	Hits	Counts	MARSE
1	2.98	-0.04	3.73	309.11	10.17489	499.00	36.00	482.00	745.02
2	3.51	-0.09	5.07	314.80	13.8621	696.00	45.00	671.00	1221.43
3	3.52	0.19	3.90	314.11	11.56398	379.00	27.00	368.00	667.77
4	0.70	-0.26	5.54	298.72	6.980348	493.00	18.00	466.00	173.51
5	1.24	0.34	5.60	309.90	9.490208	678.00	40.00	646.00	420.06
6	1.93	-0.07	5.60	309.55	10.70958	648.00	37.00	620.00	624.26
7	9.88	-0.27	4.86	323.21	21.18543	541.00	42.00	530.00	2674.14
8	9.39	-0.07	4.26	323.21	21.08425	597.00	31.00	586.00	2802.50
9	2.52	-0.07	5.99	315.71	13.85822	590.00	35.00	573.00	743.74
10	2.45	-0.64	7.81	310.83	13.74087	699.00	50.00	673.00	857.90
11	2.66	-0.30	3.45	307.79	10.98403	502.00	33.00	492.00	668.85
12	1.87	-0.17	6.75	310.12	12.10061	698.00	36.00	665.00	652.07
13	0.64	0.39	4.27	298.62	5.785545	569.00	42.00	539.00	182.32
14	0.79	0.13	4.79	302.02	6.708478	789.00	47.00	738.00	312.84
15	1.02	0.11	5.10	306.35	8.769965	899.00	58.00	861.00	459.19
16	2.27	0.15	5.15	311.90	10.8641	774.00	49.00	744.00	879.75

arrowed in Fig. 4) are separately portrayed in Fig. 7. It may be noticed that every extracted AE segment exhibits a sequence

of the following patterns. (1) Each AE spike initially appears stationary and devoid of bursts (as shown within the red boxes



Fig. 8 Successive screenshots that contain the pixel value as the criterion to indicate the behavior change in the cutter for Spike 7 in the cutting process with $v=6$ m/min and $FOA=90^\circ$.

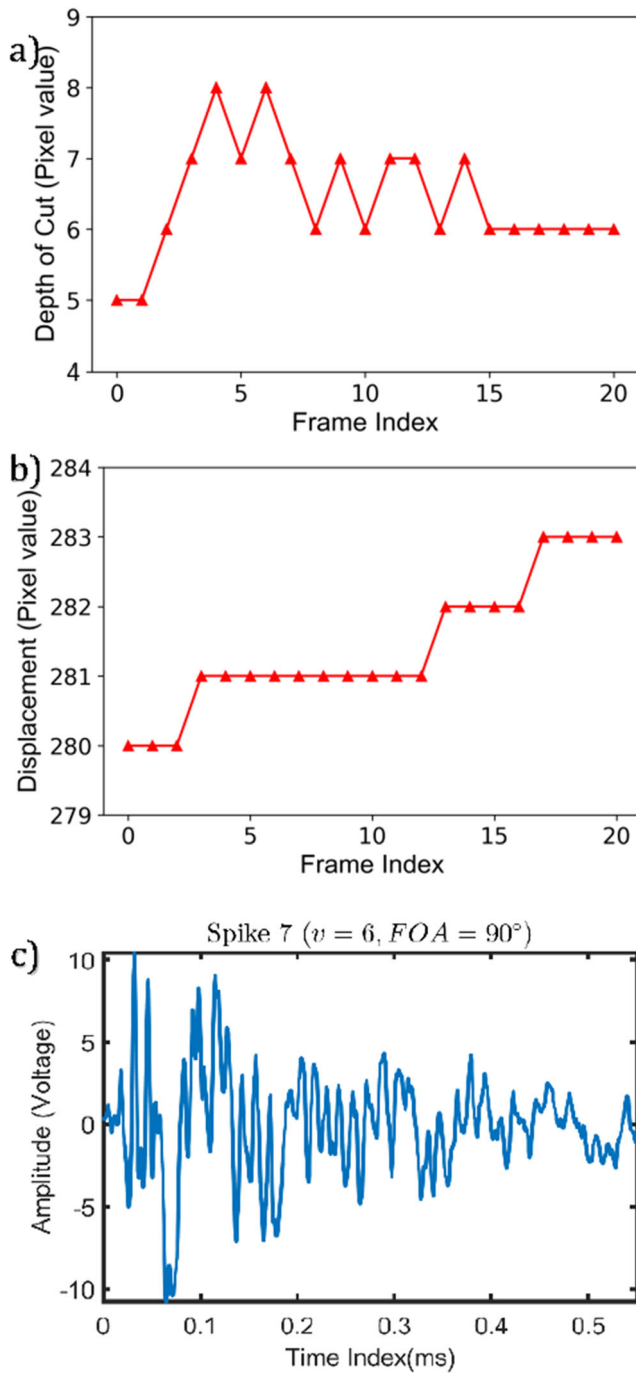


Fig. 9 Comparisons of DoC, tool displacement, and AE waveform in Spike 7 under the condition $v=6$ m/min and $FOA=90^\circ$. Here a and b, respectively, record the DoC and the tool displacement (in pixel values) extracted from HSC screenshots and synchronously aligned with c the AE waveform in Spike 7

for all plots of the spikes in Fig. 7). Such segments have relatively lower amplitudes. (2) Next is a sudden sharp rise to the peak in amplitudes, after which the AE waveform oscillates between maxima and minima (green-circled in the plots). These characteristic sharp increments and decrements (in amplitudes) generally take place over ~ 0.1 ms interval(s).

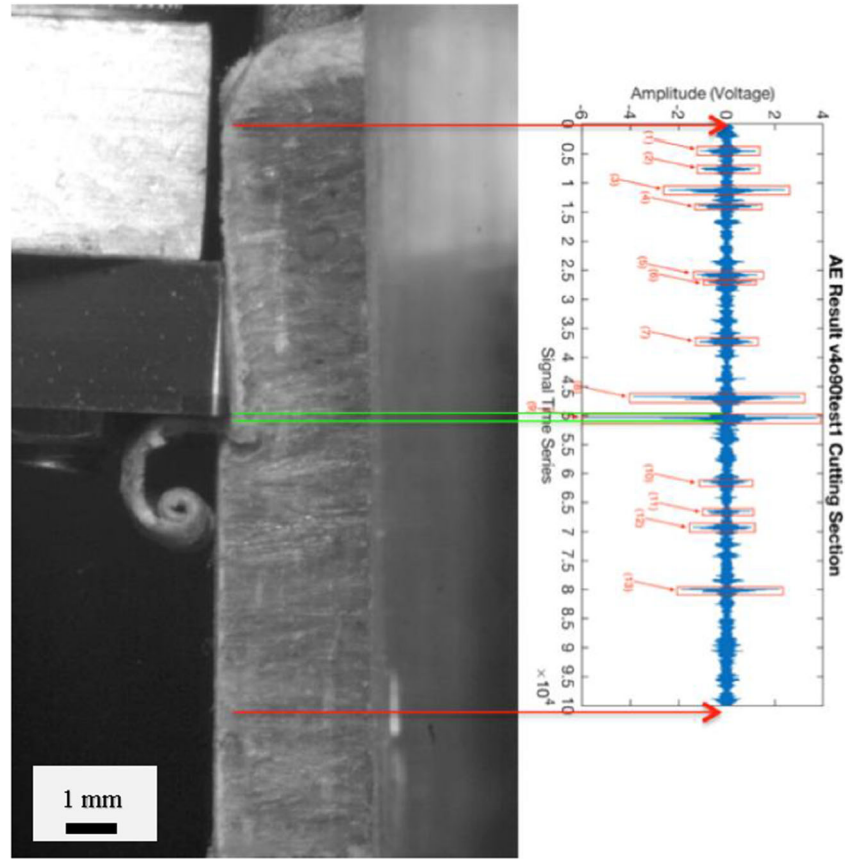
(3) The remaining tail consists of an oscillatory segment with a much smaller signal envelope (marked by the pink boxes), and its amplitudes decrease till the end of the AE event. This smooth transition from sharp peaks/valleys to subsequent oscillated tailing is often without distinguishable separating boundaries.

As observed from Fig. 7, a majority of the AE spikes follow one or the other of two distinct patterns. Two representative waveforms (Spikes 2 and 4) are examples: given similar time durations (\sim ms), Spike 2 contains fewer impulses but in higher amplitudes compared to Spike 4, whose waveform exhibits a pattern with continuous and smooth oscillations. Hereinafter the pattern in Spike 2 is referred to as Type I, and the waveforms with continuous and smooth oscillations in Spike 4 are referred to as Type II. As suggested by Fig. 7, Spikes 1–3, 7, and 16 exhibit the Type I pattern, while Spikes 4–6, 11, and 13 possess the signature of Type II. Other waveforms consist of both patterns. As suggested by Table 1, Type I waveforms may also possess higher variance (>2.5). Pertinently, one may notice that the microdynamics process that releases Type I waveforms has significantly higher AE energy than that of the Type II waveforms.

To quantify this observation, a statistical pattern analysis was carried out on these AE waveforms. Various features listed in Table 1 describe AE characteristics, for example, statistical features in different moments such as variance, skewness, and kurtosis describe their manifold distributions of the waveforms. The term *amplitude*, i.e., the largest peak (usually measured in Volts), indicates the range of an AE spike. In general, this metric converts amplitude to decibel values by a reference amplitude (commonly selected as $1\mu V$) [26]. The term *range* [or peak-to-peak (PTP) value] refers to the range/maximum voltage change in the AE signals. The *duration* is the interval between the starting and ending points where the amplitudes cross the thresholds. This feature represents the time lapse of an AE event without interference from environmental noise. The term *counts* refers to the number of pulses emitted by the measurement circuitry. *Hits* represents the total number of AE events counted within the waveform. The following procedures allow the generation of particular AE features [27]: it first generates a function to detect the AE waveforms, which are portrayed in a threshold envelope to determine *Hits* and *Counts*. The measured area of the rectified signal envelope (MARSE) is a metric measuring the area under the waveform envelope, which is regularly used in measuring AE signal strength.

One may notice that compared to other features, PTP values and MARSE along with the variance enable us to differentiate among different types of waveforms. For Type I waveform patterns, MARSE values (~ 600 to 1200) are significantly higher than for those of Type II (less than 600). In addition, PTP values (along with the variance) suggest a larger range of amplitude and its variations in Type I than in Type II, with continuous oscillation. However, features such as

Fig. 10 The red arrows show the start and end points of the cutting process in the video, and the green parallel lines show the start and end points of the successive screenshots taken of Spike 9 during NFRP machining under condition $v=4\text{m/min}$ and $FOA=90^\circ$.



Kurtosis, *Hits*, and *Counts* are not noticeably different between the two types of waveforms.

As noted earlier, the recording under the condition of $v = 6 \text{ m/min}$ and $FOA = 90^\circ$ acquired $\sim 100,000$ total data points (the process lasted for about 100 ms). The cutting process in the HSC video started at 3.2s and ended at 14.4s. Fig. 8 presents successive screenshots from the start to the end of Spike 7, with the tool tip location in the cutting process specified in pixel values. The variations in DoC and tool tip displacement along the cutting direction (in pixel values) are plotted in Fig. 9 a and b with synchronously aligned AE spikes shown in Fig. 9c. It may be noticed that the AE waveform reaches its highest peaks/valleys in Spike 7 (see Fig. 9 c) when a sudden increase in DoC occurs. On the other hand, the AEs exhibit continuous waveform patterns (smooth oscillation without sharp peaks and/or valleys) when the DoC's are relatively constant (as suggested by the tail part of Spike 7 shown in Fig. 9 a and c).

From observing the recording snapshots before and after this spike, one can notice that an abrupt change in DoC occurs because the cutting tool tip penetrates the workpiece surface, which results in a possible sharp increase in cutting force and in turn introduces a stagnant motion (or freeze-and-release motion) during the NFRP machining. Evidence can be found in Fig. 9b: this segment (frame 4 to frame 13) has a constant displacement right after the abrupt increase in the DoC,

suggesting that a stagnant/freeze motion is introduced because the cutting tool penetrates and the resultant increase in uncut materials [with random bundle(s) of the reinforced elements] prevents a smooth and stable cut. After the cutting tool penetrates the material, the tool tip goes back to its original position before Spike 7 emerges, and the DoC decreases to its original value. As a result, because there is less uncut material, the AE waveform decreases after a certain number of oscillations. Hence, the uncut material (and associated chip flow) plays a significant role in the resulting AE waveform pattern.

Another case study under different cutting conditions ($v = 4 \text{ m/min}$ and $FOA = 90^\circ$) is also presented. It may be noticed that the Type I pattern of the AE waveform generated due to the freeze-and-release motion is prevalent in most of the NFRP cutting process case studies, especially under these conditions with $FOA = 90^\circ$. The screenshots of the HSC recording along with the synchronized AE signals are shown in Fig. 10. Of the 13 spikes detected, Spike 9 under this condition ($v = 4 \text{ m/min}$ and $FOA = 90^\circ$) is selected to show the connections of the tool-workpiece interface to AE signal generation.

The spikes under $v = 4 \text{ m/min}$ and $FOA = 90^\circ$ can also be characterized/classified into two major types as previously introduced. Recall that Type I has sharp peaks and valleys, while Type II spikes have fewer bursty oscillations with a longer decay time. In this case study, each type of spike is presented in the

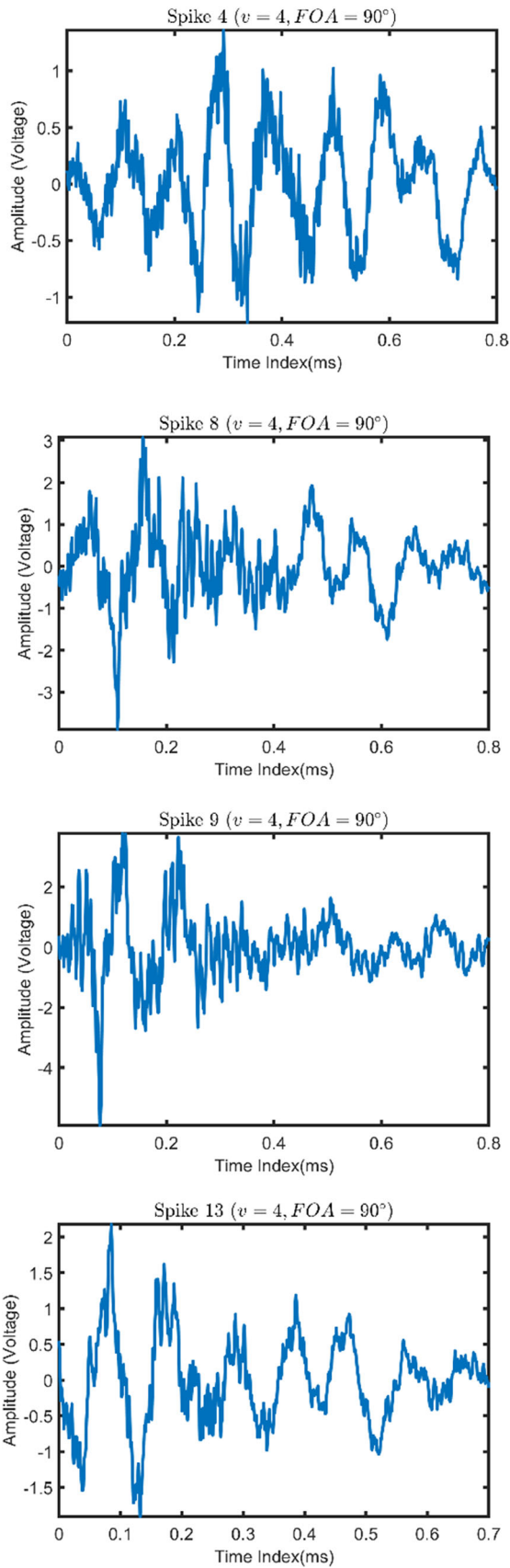


Fig. 11 A collection of spikes belonging to Type I pattern from the cutting process under $v=4\text{m/min}$ and $FOA=90^\circ$.

same group (Fig. 11 presents the Type I spikes and Fig. 12 Type II spikes under $v=4\text{ m/min}$ and $FOA = 90^\circ$).

Table 2 presents all extracted feature values for all collected spikes. The spikes in green rows belong to Type I waveform, while those shaded in salmon have the Type II pattern. The spikes without shading generally possess characteristics of

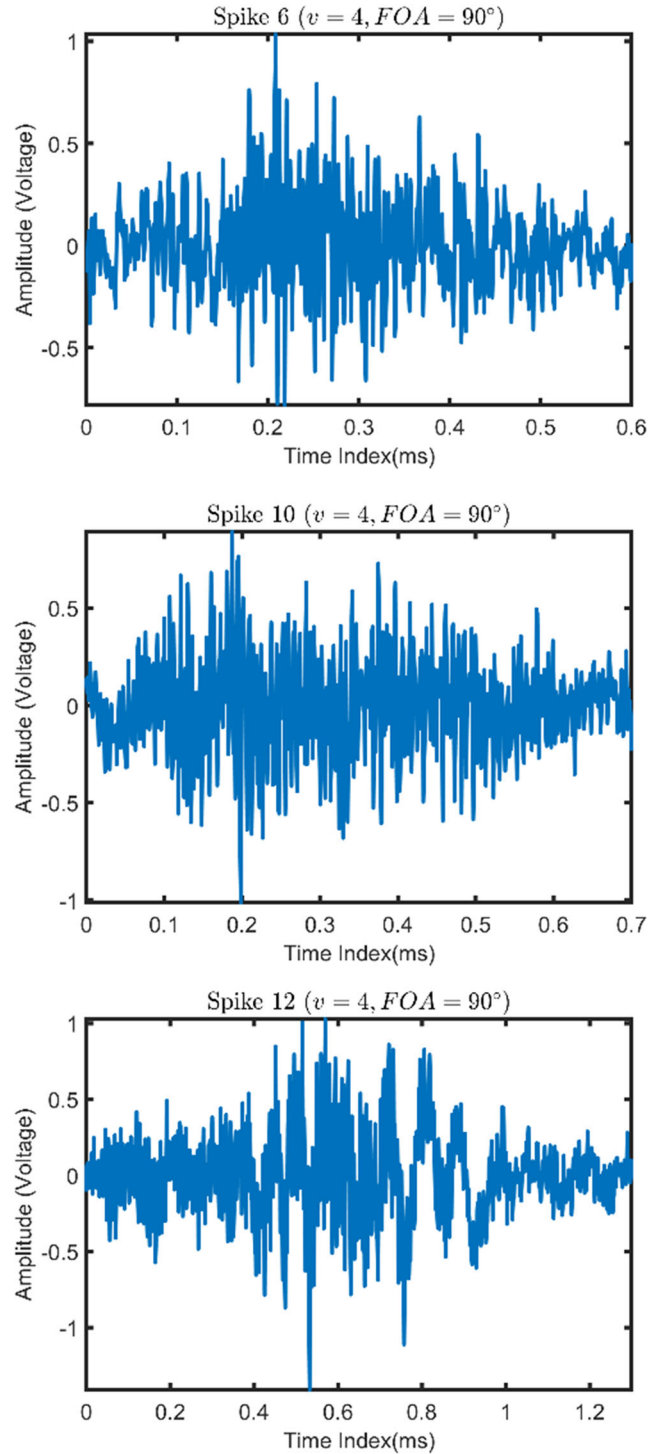


Fig. 12 Type II spikes from the cutting process with $v=4\text{m/min}$ and $FOA=90^\circ$.

Table 2 A summary of the extracted features of all collected spikes under $v = 4\text{m/min}$ and $FOA = 90^\circ$, where the two different colored shadings represent distinct waveform patterns (Types I and II). The rows with no shading contain spikes with both types of waveform patterns

Spike no.	Variance	Skewness	Kurtosis	Amplitude	Range	Duration	Counts	MARSE
1	0.1512	0.0907	3.2120	280.0257	2.338528	476	26	427
2	0.1529	0.0126	3.1124	279.2372	2.263853	680	31	609
3	0.4297	0.0239	1.6856	294.1025	4.839337	849	40	785
4	0.2152	-0.0242	2.6525	282.4499	2.587122	794	37	724
5	0.1617	0.0597	3.2290	281.2896	2.545743	740	35	667
6	0.0548	0.3515	4.4252	276.9748	1.814832	592	26	471
7	0.0849	-0.0684	3.7379	278.1232	2.26256	1193	49	1005
8	0.7322	-0.1643	4.6834	298.782	6.968063	745	45	707
9	1.2090	-0.2125	7.2403	302.9267	9.712617	799	51	768
10	0.0665	-0.0287	3.4880	274.007	1.903085	695	29	572
11	0.0625	0.2148	4.7046	276.2293	1.835521	894	33	690
12	0.0769	-0.0273	4.5011	276.8493	2.436478	1298	60	1046
13	0.3818	0.0602	3.5835	291.862	4.084504	695	43	642

both types of AE waveforms. Based on investigations into multiple experimental case studies, one may conclude that the approach presented here can identify AE waveform patterns related to the microdynamics of the NFRP machining process. Essentially, the relationships between AE waveform patterns and DoC's and the cutting tool displacement have similar features/patterns as the results shown in the previous case study: the peaks and/or valleys (after rise time) in the waveform envelopes are mainly due to the sudden increase in the DoC. As suggested by Fig. 13b, the displacement along the cutting direction increases, with several freeze-and-release motions in the cutting direction.

More importantly, the results from the synchronous analysis approach suggest that the freeze-and-release motion, as one result of the inconsistent cutting velocity, variations in the depth of cut (DoC), and the heterogeneity of the material microstructure, is one major cause for the AE waveform pattern generated during the NFRP machining. Intuitively speaking, NFRP machining holds certain analogies to the tilling or shovelling a packed soil containing entrenched distribution of roots and weeds. Type I AE released from an NFRP machining process is analogous to the "shock" wave generated whenever the tool hits and cuts through a weed and entrenched root during this process. These physical mechanisms, as captured by these AE patterns, hold significant bearing on the quality of the NFRP machined surfaces [12]. These findings therefore open up an opportunity to track AE signals to assess the effective cutting energy and the resultant surface integrity that are affected by these unsteady motion patterns.

5 Summary and discussions

This paper presents a comprehensive characterization of specific AE waveform patterns in NFRP manufacturing. The

contributions reported in the paper that have led to direct observation of a physical source of a prominent AE waveform pattern are as follows.

1. An experimental study was performed to investigate the NFRP machining process and the resulting AE waveforms at a microsecond time scale and micrometer length-scale resolutions. High-speed camera recordings are synchronized with sensor signals gathered during the two-dimensional machining process. The approach reveals the connections between the microdynamics of orthogonal cutting processes for NFRPs and the AE patterns over a 10^{-2} – 10^{-5} s range and 10^{-5} – 10^{-6} M range. The resolutions of AE RMS signals, which are more commonly used in machining process monitoring, would be inadequate to capture the waveform patterns and spatio-temporal resolutions achieved in the present work.
2. During the orthogonal cutting of NFRPs, at least two prominent AE waveform burst patterns (Type I and Type II) were observed. Based on correlating the images with the waveform patterns, acoustic emission release in NFRP machining can be attributed to multiple sources, such as the microdynamics associated with changes in the tool-workpiece interface geometry, chip formation and entanglement on the tool rake and flank faces, and subtle changes in the microstructure of uncut materials (resulting in variations in localized machining characteristics) [12]. All of these sources may not only influence AE waveform responses, but have a direct bearing on the surface quality.
3. The relationship between the time domain characteristics of AE signals and the fundamental microdynamics of the NFRP cutting processes was investigated in the experimental studies. The AE waveforms exhibit two distinct behaviors (Type I: continuous wave and Type II: bursty

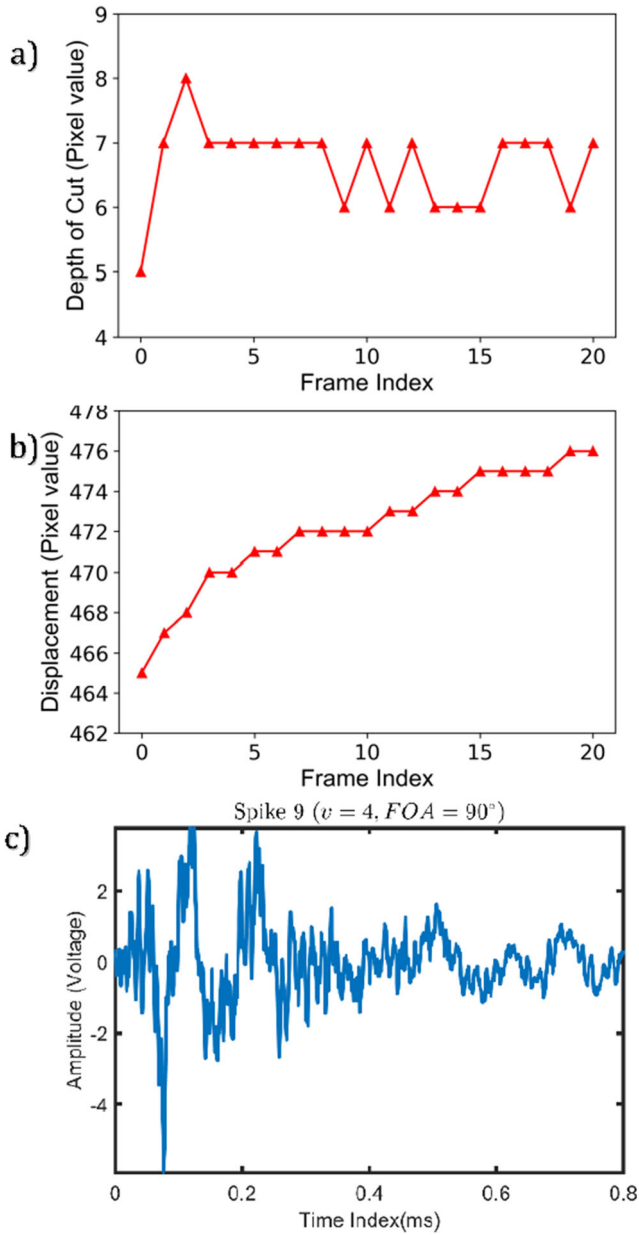


Fig. 13 Comparisons of DoC, tool displacement, and AE waveform of Spike 9 under the condition of $v=4$ m/min and $FOA=90^\circ$. Here a records the DoC and b tool displacement in the cutting direction extracted from HSC screenshots. Pixel values are time-synchronized with c the AE waveforms of Spike 9

patterns). Among all time domain features extracted, *MARSE*, *Range*, and statistical feature variance are significantly higher for Type I waveforms compared to the Type 2 AE waveform patterns. This result further indicates that the underlying physical mechanisms for the generation of these two types of waveforms may be different.

4. NFRP machining dynamics introduces sudden changes in the depth of cut (DoC) and, consequently, changes in the tool-workpiece interface geometry. In addition, the

variations in the microstructure (multi-scale structure of the fibers and their random distribution within the matrix) create heterogeneity in its localized mechanical properties. All of these factors introduce a unique freeze-and-release motion during the orthogonal cutting that contributes. The synchronous analysis of images and signals suggests that the Type I AE waveform bursts consistently are marked by a freeze-and-release motion of the tool during NFRP machining.

5. Very few of the prior investigations have focused on deciphering the physical sources of AE in real time during the machining processes [28]. This is due to the lack of a synchronous analysis tool to practically trace the generation of AE waveforms in real time. The analytic tool presented in this study utilizes an in-process sensing technology combined with HSC recordings, which allows a synchronized analysis of the HSC recordings with point-to-point AE events to investigate the sources of different AE waveform patterns, viz., Types I and II of AE spikes, during orthogonal cutting processes.

For future work, to extend the current work to different machining processes (e.g., different types of machine tooling as well as variant tool geometries), the impacts of the tool geometry and the coupling effects on the system dynamic behaviors due to the rotary tools need to be further investigated. In addition, the random effects on the microstructure of NFRPs (e.g., fiber packing density and random distribution within the matrix basis) as well as chip entanglement during machining need to be incorporated for the decoupling of the AE waveform pattern from each source and investigating the machinability of the heterogeneous NFRPs. An assessment of the quality of the machined subsurface can then be developed with the goal of extending the application of smart AE sensing for evaluating the achieved surface at the micro(meter)-level.

Author contribution Zimo Wang conducted experiments, collected experiment results, developed data analysis, and wrote and edited the manuscript; Ruiqi Guo analyzed experiment results and contributed the analysis of the microdynamics and its relationship with AE signal nature; Qiyang Ma edited paper and analyzed the data and visualized the results; Faissal Chegdani designed and conducted experiments; Bruce Tai realized the hardware setup and designed experiments; Mohamed El Mansori and Satish T.S. Bukkapatnam supervised the work and edited the paper. All the authors reviewed and edited the final document.

Funding This research is supported by the National Science Foundation (NSF) (S&AS: INT #1849085), X-grant program at TEES.

Availability of data and material The datasets generated during and/or analyzed during the current study are available from the corresponding author on reasonable request.

Declarations

Ethical approval The authors claim that there are no ethical issues involved in this research.

Consent to participate Not applicable. The article involves no studies on humans or animals.

Consent to publish Not applicable. The article involves no studies on humans or animals.

Competing interests The authors declare no competing interests.

References

1. Mohammed L, Ansari MN, Pua G, Jawaid M, Islam MS (2015) A review on natural fiber reinforced polymer composite and its applications, *International Journal of Polymer Science* 2015
2. Chegdani F, Wang Z, El Mansori M, Bukkapatnam ST (2018) Multiscale tribo-mechanical analysis of natural fiber composites for manufacturing applications. *Tribol Int* 122:143–150
3. De Rosa IM, Santulli C, Sarasini F (2009) Acoustic emission for monitoring the mechanical behaviour of natural fibre composites: a literature review. *Compos A: Appl Sci Manuf* 40(9):1456–1469
4. Chegdani F, Takabi B, Tai BL, El Mansori M, Bukkapatnam ST (2018) Thermal effects on tribological behavior in machining natural fiber composites. *Proc Manuf* 26:305–316
5. Chegdani F, Mezghani S, El Mansori M (2015) Experimental study of coated tools effects in dry cutting of natural fiber reinforced plastics. *Surf Coat Technol* 284:264–272
6. Chegdani F, Mezghani S, El Mansori M, Mkaddem A (2015) Fiber type effect on tribological behavior when cutting natural fiber reinforced plastics. *Wear* 332:772–779
7. Babu GD, Babu KS, Gowd BUM (2013) Effect of machining parameters on milled natural fiber-reinforced plastic composites. *J Adv Mech Eng* 1:1–12
8. Teti R, Jemielniak K, O'Donnell G, Dornfeld D (2010) Advanced monitoring of machining operations. *CIRP Ann-Manuf Technol* 59(2):717–739
9. Al-Dossary S, Hamzah RR, Mba D (2009) Observations of changes in acoustic emission waveform for varying seeded defect sizes in a rolling element bearing. *Appl Acoust* 70(1):58–81
10. Baccar D, Söfker D (2017) Identification and classification of failure modes in laminated composites by using a multivariate statistical analysis of wavelet coefficients. *Mech Syst Signal Process* 96:77–87
11. Terchi A, Au Y (2001) Acoustic emission signal processing. *Measurement Control* 34(8):240–244
12. Wang Z, Chegdani F, Yalamarti N, Takabi B, Tai B, Mansori ME, Bukkapatnam ST (2020) Acoustic Emission (AE) characterization of natural fiber reinforced plastic (NFRP) composite machining using a random forest machine learning model. *J Manuf Sci Eng* 1–40
13. Blum T, Inasaki I (1990) A study on acoustic emission from the orthogonal cutting process. *J Eng Ind* 112(3):203–211
14. Rabani A, Marinescu I, Axinte D (2012) Acoustic emission energy transfer rate: a method for monitoring abrasive waterjet milling. *Int J Mach Tools Manuf* 61:80–89
15. Kannatey-Asibu E Jr, Dornfeld D (1982) A study of tool wear using statistical analysis of metal-cutting acoustic emission. *Wear* 76(2):247–261
16. Diei E, Dornfeld D (1987) Acoustic emission sensing of tool wear in face milling. *J Eng Ind* 109(3):234–240
17. Dornfeld D, Handy C (1987) Slip detection using acoustic emission signal analysis, *Proceedings. 1987 IEEE International Conference on Robotics and Automation, IEEE*, pp 1868–1875
18. Diniz A, Liu J, Dornfeld D (1992) Correlating tool life, tool wear and surface roughness by monitoring acoustic emission in finish turning. *Wear* 152(2):395–407
19. Bukkapatnam ST, Kumara SR, Lakhtakia A (1999) Analysis of acoustic emission signals in machining. *J Manuf Sci Eng* 121(4):568–576
20. Chang D-C, Bukkapatnam S (2004) Towards characterizing the microdynamics of AE generation in machining. *Mach Sci Technol* 8(2):235–261
21. Wang Z, Dixit P, Chegdani F, Takabi B, Tai BL, El Mansori M, Bukkapatnam S (2020) Bidirectional gated recurrent deep learning neural networks for smart acoustic emission sensing of natural fiber-reinforced polymer composite machining process smart and sustainable manufacturing systems (In press)
22. Haggui M, El Mahi A, Jendli Z, Akrouit A, Haddar M (2019) Static and fatigue characterization of flax fiber reinforced thermoplastic composites by acoustic emission. *Appl Acoust* 147:100–110
23. Barile C, Casavola C, Pappalettera G, Kannan VP (2020) Application of different acoustic emission descriptors in damage assessment of fiber reinforced plastics: a comprehensive review. *Eng Fract Mech* 2020:107083
24. Mi Y, Chen Z, Wu D (2018) Acoustic emission study of effect of fiber weaving on properties of composite materials, 2018 IEEE International Ultrasonics Symposium (IUS), IEEE, pp 1–4
25. Mao R-S, Huang Z-M, Wang Z-W (2021) Predicting strength of a unidirectional composite containing interface crack. *Compos Sci Technol* 207:108665
26. Gholizadeh S, Leman Z, Baharudin B (2015) A review of the application of acoustic emission technique in engineering. *Struct Eng Mech* 54(6):1075–1095
27. Unnpörsson R (2013) Hit detection and determination in AE bursts. *Acoust Emission-Res Appl* 1–20
28. Kishawy H, Hegab H, Umer U, Mohany A (2018) Application of acoustic emissions in machining processes: analysis and critical review. *Int J Adv Manuf Technol* 98(5-8):1391–1407

Publisher's note Springer Nature remains neutral with regard to jurisdictional claims in published maps and institutional affiliations.